

Freestanding fiber mats of zeolitic imidazolate framework-7 via one-step scalable electrospinning

Seongpil An^{1,a)}, Ji Sun Lee^{2,3,a)}, Bhavana N. Joshi¹, Hong Seok Jo¹, Kirill Titov⁴, Jong-San Chang^{2,5}, Chul-Ho Jun³, Salem S. Al-Deyab⁶, Young Kyu Hwang^{2,b)}, Jin-Chong Tan^{4,b)}, Sam S. Yoon^{1,b)}

¹School of Mechanical Engineering, Korea University, Seoul 02841, Republic of Korea

²Research Group for Nanocatalysts, Korea Research Institute of Chemical Technology, Daejeon 34114, Republic of Korea

³Department of Chemistry, Center for Bioactive Molecular Hybrid, Yonsei University, Seoul 03722, Republic of Korea

⁴Department of Engineering Science, University of Oxford, Parks Road, Oxford OX1 3PJ, United Kingdom

⁵Department of Chemistry, Sungkyunkwan University, Suwon 16419, Republic of Korea

⁶Department of Chemistry, Petrochemical Research Chair, College of Science, King Saud University, Riyadh 11451, Saudi Arabia

Abstract

We demonstrated fabrication of freestanding zeolitic imidazolate framework (ZIF)-7 nanofiber mats by means of one-step scalable electrospinning. Formation of ZIF-7 nanoparticles embedded in polymer fibers has been unambiguously pinpointed *via* X-ray diffraction, transmission electron microscopy, and adsorption studies. The nanofiber mats exhibited excellent characteristics with the average diameter of 245 nm in adsorption and desorption of carbon dioxide, making them attractive for gas separation and other selective filtration applications. This excellent property of the ZIF-7 mats is explained with the gate-opening phenomenon of ZIF-7 that yielded a stepwise rise in overall carbon dioxide uptake capacity. The mechanical strength of the nanofiber mats was also obtained via large-strain uniaxial tensile deformation, which enabled preliminary assessment of the mat's suitability in textiles and membranes targeting separation and filtration applications with large-area permeability.

Keywords: Electrospinning, metal-organic frameworks, ZIF-7, CO₂ capture

¹These authors contributed equally.

Introduction

Advancement in modern industry and society increases fossil fuel consumption dramatically which in turn increases greenhouse gas emissions.¹ According to the prediction of the Intergovernmental Panel on Climate Change (IPCC),² the rise in the CO₂ concentration in environment will increase the global temperature by 1.9 °C. Thus, developing new technology capable of capturing CO₂ is becoming an urgent issue. Various techniques have been developed for anthropogenic CO₂ capture, such as amine-solvent scrubbing, cryogenic distillation, solid sorbents etc.^{3,4} In this context, metal-organic frameworks (MOF) have recently generated considerable research interest due to their well-ordered pore structure, high surface area, flexible dynamic behavior in response to guest molecules, and designable functionalization of the channel surfaces. These unique combination of material properties provides an exciting potential for CO₂ capture applications.⁵ These qualities of MOF also offer various other applications, such as gas storage and purification,⁶ catalysis⁷, molecular recognition, and drug delivery.⁸

Zeolitic imidazolate framework (ZIF) is a topical family of MOF material, constructed by coordinating imidazole-based organic linkers and zinc tetrahedra (ZnN₄) to produce a myriad of porous frameworks mimicking the topology of zeolites (aluminosilicates).⁹ ZIFs are highly versatile and potentially useful for various applications because of their good chemical stability,⁹ in conjunction with its tunable pore structures conferring wide ranging mechanical properties¹⁰ and intriguing framework dynamics,¹¹ thereby attracting considerable interest in the fields of gas separation, gas sensors,^{12,13} catalysis,^{14,15} and biotechnology.¹⁶ Recent studies have established that ZIFs (including ZIF-7, ZIF-8, and ZIF-68) exhibit a relatively high thermal stability of up to 673 K.¹⁷ The pore

aperture (window) of ZIF-7 and ZIF-8 estimated by crystallographic data are about 0.3 nm and 0.34 nm, respectively,¹⁸ values which correspond to the molecular sizes of H₂O (0.265 nm), H₂ (0.289 nm), CO₂ (0.305 nm), and N₂ (0.364 nm).¹⁹ Like in the case of zeolites, the kinetic separation of C₂ (ethane/ethylene) and C₃(propane/propylene) was successfully demonstrated by utilizing the small-sized windows of ZIF-7 and ZIF-8.²⁰ Noteworthy, ZIF-7 has high window flexibility towards a pressure stimulus, resulting in improved sorption characteristics to afford H₂ and CO₂ separations;²¹ likewise this flexibility opens up new applications in gas separation, such as to accommodate N₂O and C₂–C₄ adsorption.⁶

Although ZIF has numerous potential applications, its industrial use requires shaping or joining processes to create modules suitable for large-scale deployments. It is generally accepted that nanocomposite structures of MOF are vital for MOF applications for two important reasons: nanocomposites comprising MOF and polymer nanofibers can be easily separated from the heterogeneous solution of adsorbent and adsorbate, and also shaped MOF can be used to realize catalytic and separation applications.²² For that purpose, many experiments have been performed to make MOF nanocomposites between MOF–MOF, MOF–inorganic materials, and MOF–organic materials including MOF–polymers.²³ Amongst them, MOF–polymer nanofibers, such as ZIF-8/polyvinylpyrrolidone (PVP)²⁴ and Cu-BTC (benzene-1,3,5-tricarboxylate)/polymers²⁵ have attracted much attention in the separation and purification of gas and liquid mixtures.²⁶ The use of nanofibers from different materials were proven to be beneficial in various applications, such as filtration, controlled drug release, anode materials, sensors, and catalysis.²² In order to increase the efficiency of filtration/gas separation, porous fibers will present clear advantages against a dense (monolithic) bulk material. Despite preceding nanofiber studies on MOF,^{24,27-30} the studies are limited on ZIF-8. While ZIF-7 [Zn(benzimidazolate)₂] is akin to ZIF-8 [Zn(2-

methylimidazolate)₂] in terms of its sodalite (SOD) topology,⁹ as mentioned above, it has a relatively smaller pore aperture (window size) thus making it particularly suitable for CO₂ capture, compared to other gases. ZIF-7 was first discovered by Huang *et al.*³¹ in 2003. Various synthesis procedures have been reported for fabricating ZIF films and membranes which can be classified into two categories: *in situ* growth and secondary (seeded) growth.²² The secondary growth method requires a seeding step in addition to the solvothermal growth step. The increased number of preparation steps makes this process very complex thus lowering its reproducibility.^{15,32,33}

Herein, we report on the fabrication of ZIF-7/polyacrylonitrile (PAN) nanocomposite fibers using the scalable method, in which ZIF-7 nanoparticles are formed during the reaction and are aligned directly with the fibers during the electrospinning process. Significantly, this synthesis route is a one-step process and it does not require cumbersome solvothermal treatments. In the present study, for the first time, we produced ZIF-7/PAN nanocomposite fibers supporting well-ordered microporous ZIF structure, which could open up new possibilities in CO₂ gas capture and separation. The mechanical properties of the MOF fibers also are very important regarding various technical applications. For example, the intrinsic porosity of ZIFs should be maintained during sorption/desorption cycles, while at the macroscale the fiber nanocomposite as a whole must be mechanically resilient to withstand stresses and strains arising from service.³⁴ Thus, characterization of the core mechanical properties of PAN and ZIF-7/PAN nanofibers has also been carried out in this work.

Experimental methods

Starting materials

Zinc nitrate hexahydrate ($\text{Zn}(\text{NO}_3)_2 \cdot 6\text{H}_2\text{O}$, 98%, Sigma-Aldrich) and benzimidazole ($\text{C}_7\text{H}_6\text{N}_2$, 98%, Sigma-Aldrich) were used as metal and ligand sources. *N,N*-dimethylformamide (DMF, 99.8%, Sigma-Aldrich) and methanol (99.8%, Samchun chemical) were used as solvent without further purification. Polyacrylonitrile (PAN, $M_w = 150$ kDa) was used as solute for the electrospinning solution.

Synthesis of ZIF-7/PAN nanofibers

Figure 1(a) shows the synthesis process of the ZIF-7/PAN solution. 8 wt% of $\text{Zn}(\text{NO}_3)_2 \cdot 6\text{H}_2\text{O}$ and 4 wt% of benzimidazole solutions in DMF were mixed, and immediately, a certain amount of PAN powder was added to the mixed solution to make 6 wt% of ZIF-7/PAN precursor. Next, the precursor was stirred at 50 °C for 3 days to crystalize ZIF-7 and, thereby, ZIF-7-containing nanofibers (NFs) could be deposited without post treatments. Specifically, regarding the case of CO_2 adsorption, different stirring temperatures of 50, 100, and 150 °C were used for the preparation to investigate whether the synthesis temperature affects the material performance.

Uniform ZIF-7/PAN NFs were electrospun onto a stainless steel substrate at 36% of humidity and under room temperature, as shown in Figure 1(b). The flow rate of 150 $\mu\text{L}/\text{h}$ was supplied by a syringe pump (Legato 100, KD Scientific Inc.) and the voltage of 7 kV was given by a high-voltage power supply (EP20P2, Glassman High Voltage Inc.). The nozzle used had 0.84 mm and 1.27 mm inner and outer diameter, respectively, and the distance between the nozzle and substrates was fixed at 10 cm.

Synthesis of ZIF-7 nanoparticles

ZIF-7 nanoparticles (NPs) were prepared by the conventional solvothermal method. Typically, a solution of benzimidazole (810 mg, 6.86 mmol) and a solution of $\text{Zn}(\text{NO}_3)_2 \cdot 6\text{H}_2\text{O}$ (1530 mg, 5.14 mmol) in 40 mL of DMF were mixed in a Teflon vessel and then reacted at 50 °C for 3 days, under the same conditions resembling the synthesis of the NFs. After the solvothermal synthesis, the products were purified by centrifugation and then washed with methanol three times to remove any unreacted reactants. Finally, the products were dried overnight below 100 °C in air atmosphere. The concentration of the reactant was similar to that used for the preparation of the electrospinning solution.

Materials characterization

To characterize and analyze the ZIF-7/PAN NFs produced, scanning electron microscope (SEM, S-5000, Hitachi, Ltd.), transmission electron microscope (TEM, JEM-2100F, JEOL Inc.), energy dispersive X-ray spectroscopy (EDS) attached to the TEM, X-ray diffraction (XRD, SmartLab, Rigaku), thermogravimetric analysis (TGA, N-1000, SCINCO M&T), CO_2 adsorption (Micromeritics), and mechanical testing (Instron tensometer) were employed. The XRD patterns were recorded on an X-ray diffractometer using $\text{Cu K}\alpha$ ($\lambda = 1.5406 \text{ \AA}$) radiation. The ZIF-7/PAN NFs samples used in SEM analysis were coated with a thin layer of platinum by an ion sputter coater before imaging. A thermogravimetric analyzer was used to determine the TGA curves with the sample held in a platinum pan under air atmosphere, using a heating rate of 5 °C/min. Moreover, CO_2 adsorption and desorption isotherms were employed to determine the porosity of the ZIF-7/PAN NFs using a volumetric adsorption apparatus (Tristar 3020, Micromeritics). Standard volumetric technique was applied to obtain the sorption data of small gas molecules in the pressure range from 5 to 760 Torr, if not otherwise specified. The sample was dehydrated at 150 °C for 3 h under high vacuum ($< 10^{-6}$ Torr) before commencing adsorption studies. Even though the pores of ZIF-7

is flexible (due to gate-opening phenomenon) enabling larger molecules to enter,¹¹ the pore size of ZIF-7 is generally smaller than the kinetic diameter of N₂ as mentioned above.³⁵ Therefore, CO₂ is selected to study the sorption characteristics of ZIF-7 crystals. In order to confirm the permanent porosity of ZIF-7/PAN NFs, here we examined the CO₂ adsorption–desorption isotherms at 196 K (-77 °C) (Figure 6). The sample cell was loaded with ~0.18 g of NF mat.

Results and Discussion

Figure 1(b) shows representative SEM images of nanofibers (NFs) being deposited after 30 s of electrospinning. The diameter of the fibers was estimated by averaging the individual values of 200 fibers, amounting to an averaged fiber diameter of 245 nm with a standard deviation of 43 nm. There is scope to tune the average diameter of the NFs by varying the polymer concentration. An image of a mat of ZIF-7/PAN NFs is shown in Figure 1(c). The mat appeared to be of milky color due to the submicron fiber size. As can be seen from Figure 1(c), we demonstrate that macroscopic nonwoven mat can be obtained at a reasonably large scale. Thus, the composite fibers can be scaled up like “MOF textile”, combining the unique properties of both polymeric fibers and MOFs simultaneously. The NFs obtained in the form of nonwoven mats were subsequently used for detailed characterizations, as described below.

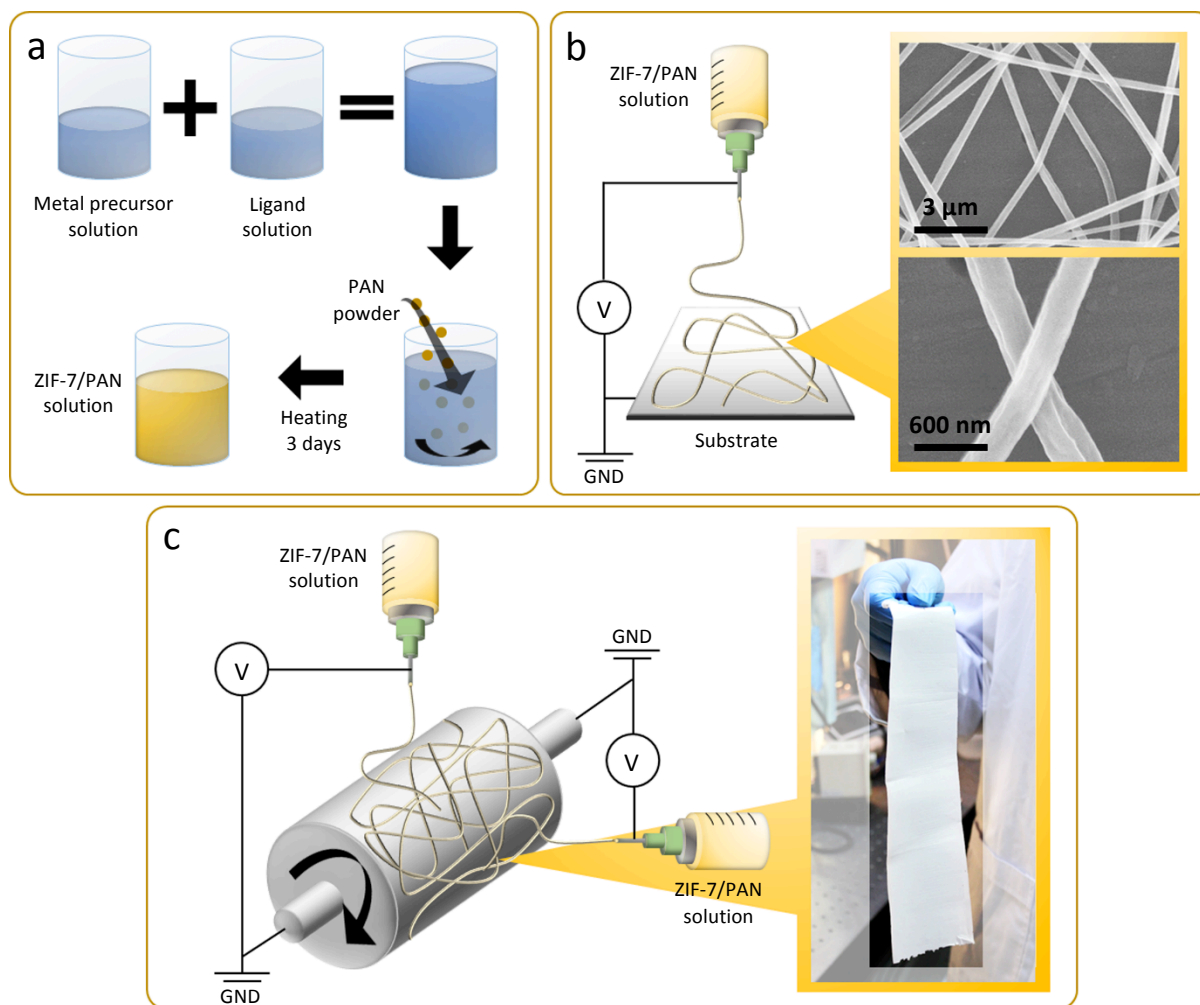


Figure 1. Schematics of (a) the synthesis process of ZIF-7/PAN solution and experimental setups used for (b) single-nozzle electrospinning including SEM images of the resulting fibers and (c) multi-nozzle electrospinning with a drum collector.

TEM studies revealed the homogeneous distribution of the ZIF-7 NPs embedded in a polymeric fiber, as shown in Figure 2(a) (top). In contrast, the neat PAN NFs in Figure 2(a) (bottom) retain a smooth and uniform surface with an average fiber diameter of 200–300 nm. The magnified TEM images of the composite ZIF-7/PAN NFs (Figure 2(b)) clearly show that the fiber surface becomes more corrugated (increased roughness) due to loading of ZIF-7 in PAN nanofiber; we also note that the distribution of ZIF-7 is homogenous to a large extent. The elemental analysis of the ZIF-7/PAN NFs carried out by TEM-EDX is presented in

Figure 3 and clearly shows that the higher concentration of carbon comes from the polymer PAN (matrix phase). Zn atoms detected *via* elemental mapping can be ascribed to the ZIF-7 NPs embedded and coated all over the fiber. The presence of other elements, particularly nitrogen (originated from PAN and ZIF-7) and oxygen (originated from water absorbed on nanofibers), were also observed at some small percentages.

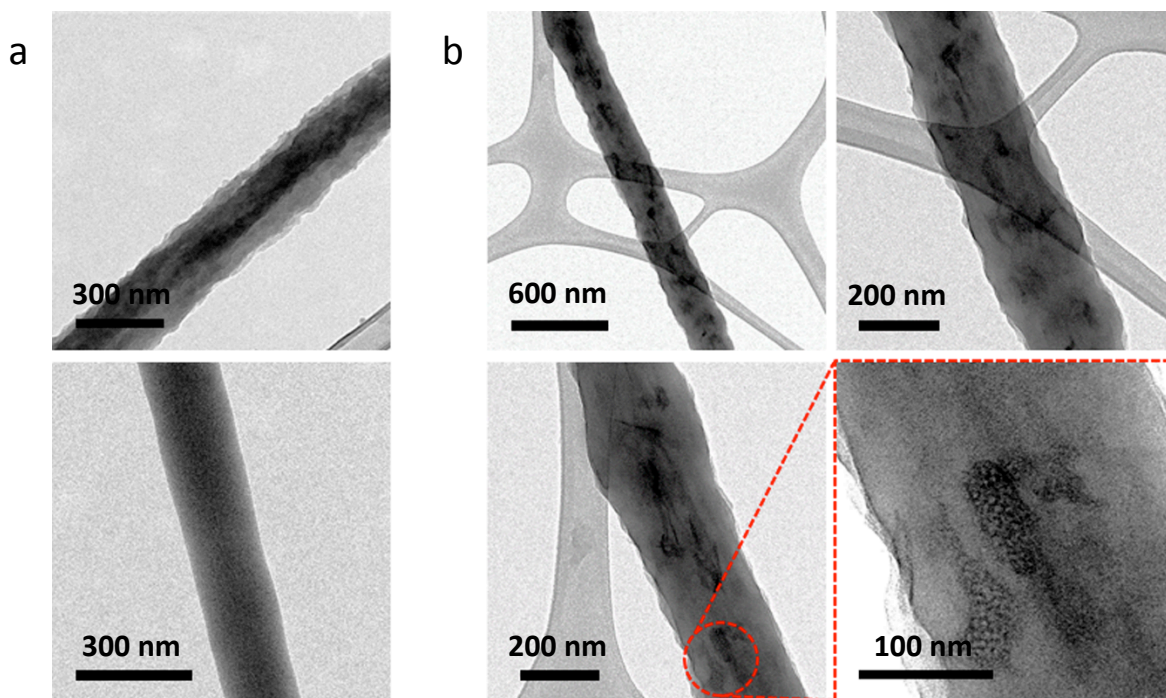


Figure 2. TEM images of (a) a single ZIF-7/PAN NF (top), and PAN NF (bottom) and (b) TEM images of ZIF-7/PAN composite NFs at various magnifications.

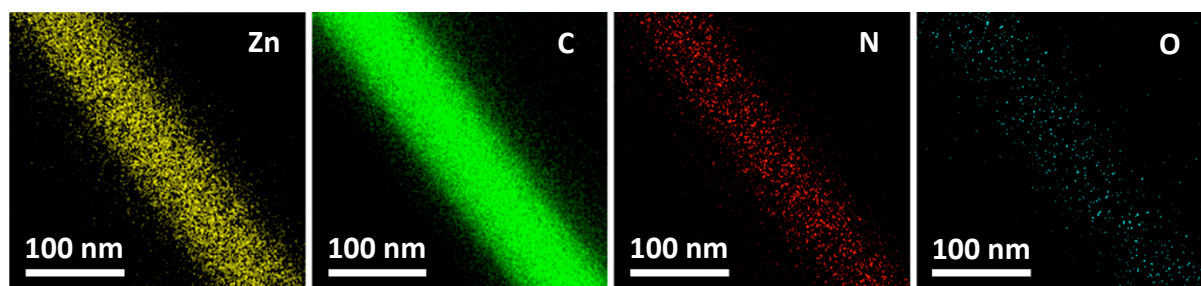


Figure 3. TEM-EDX elemental mapping of ZIF-7/PAN NFs.

Figure 4(a) shows the XRD patterns of pristine ZIF-7 NPs, PAN NFs, and ZIF-7/PAN NFs. The ZIF-7 pattern exhibits the characteristic ZIF-7 peaks at $2\theta = 7.15^\circ$, 7.65° , 10.5° , 12.09° , 13.03° , 15.37° , 18.64° , 19.60° , 21.1° , and 23° .³⁶ The broad and dominant peak of PAN around 17° corresponds to the orthorhombic (110) orientation in the case of PAN NFs.³⁷ PAN along with ZIF-7 peaks are clearly observed for the composite fibers which confirms the successful spinning of ZIF-7/PAN NFs. Additionally, XRD patterns of other synthesis temperatures of 100 and 150 °C cases have been considered, and the data suggest that the overall crystallization of ZIF-7 in the nanofibers increases as the synthesis temperature rises as depicted in Figure 4(a). This synthesis temperature effect is also demonstrated in the CO₂ adsorption result. Figure 4(b) shows the effect of three different annealing temperatures on the ZIF-7/PAN NF mat (which was synthesized at 50 °C). The sample was heated from room temperature to 200 or 400 °C for 1 h at a heating rate of 5 °C/min in argon atmosphere. The figure clearly shows that ZIF-7 retains its structure up to 200 °C, however, it degrades at 400 °C (thermal amorphisation).³⁸ At 400 °C, diffraction peaks corresponding to ZIF-7 structure are no longer discernible; the peak generated at 35° (belonging to ZnO as per JCPDS card 36-1451) confirms that ZIF-7 has been converted to ZnO. To better verify the conversion, XRD analyses of ZIF-7 NPs (without PAN) as different annealing temperatures were conducted (Supplementary Information, Figure S2) and thus showed clear ZnO peaks at 400 °C, which corresponds to planes (100), (002), and (101). The PAN peak at 17° in Figure 4(b) is becoming sharper with enhanced intensity due to its increased crystallinity. In the case of ZIF-8, Du *et al.*³⁹ reported similar results at 300 °C and above for long annealing times of more than 1 h.

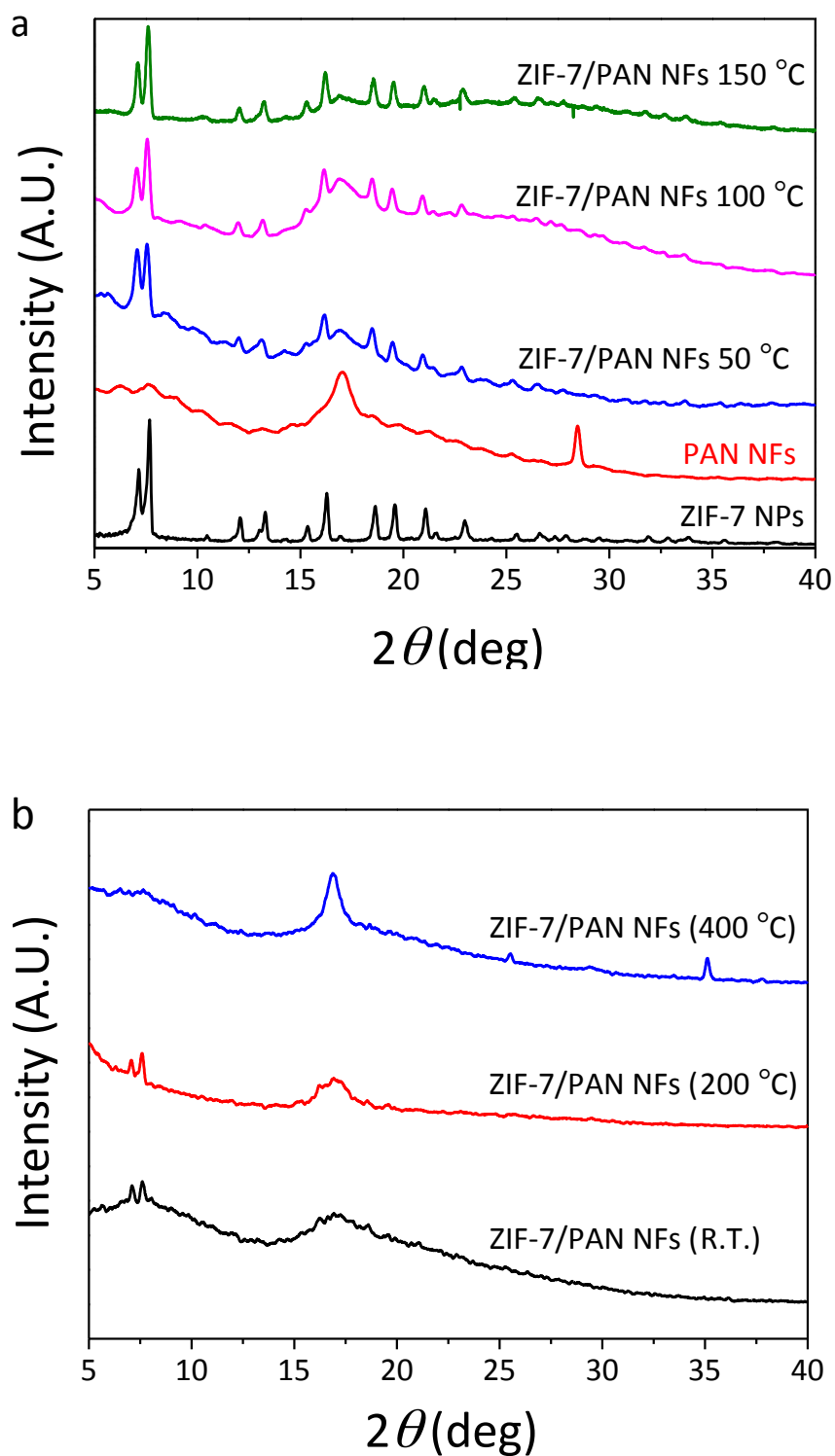


Figure 4. XRD patterns of (a) ZIF-7/PAN at different synthesis temperatures of 50, 100, and 150 °C, PAN NFs, and ZIF-7 NPs and (b) ZIF-7/PAN NFs annealed at different temperatures.

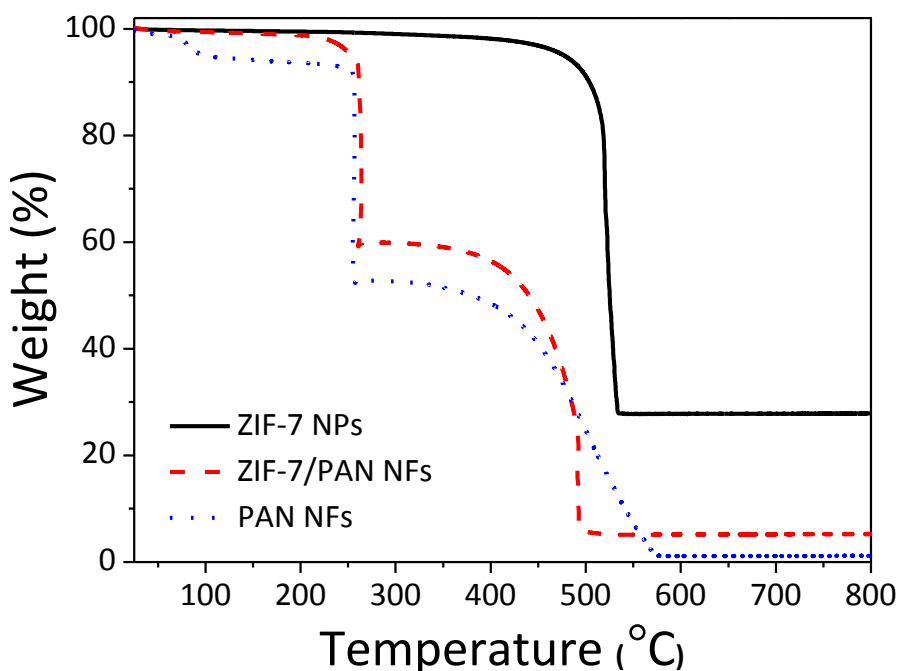


Figure 5. TGA analysis of ZIF-7 NPs and ZIF-7/PAN NFs under air atmosphere.

The thermal stability of pristine PAN NFs, ZIF-7/PAN NFs, and ZIF-7 NPs synthesized by the solvothermal method under atmospheric air is presented in Figure 5. In the case of ZIF-7/PAN NFs, two important weight-loss regions were identified between the temperatures of 25 and 800 °C. Approximately 40% of weight loss is observed between 25–375 °C, resulting from the removal of guest solvents such as H₂O, methanol, and DMF³⁶ which increases the porosity of ZIF-7/PAN NFs. The second important weight loss of about 54.8% is observed between 400–500 °C and reflects the thermal decomposition of the structural framework of ZIF-7/PAN NFs, associated with the decomposition of the organic linkers and this is accompanied by formation of ZnO. Thus, the TGA analysis proves that the fabricated ZIF-7/PAN NFs are thermally stable up to ~400 °C, thereby consistent with the XRD results presented above. Furthermore, the chemical composition of the ZIF-7 NPs in the NFs was deduced by comparing the amount of remaining ZnO (above 600 °C) of these NPs

with that of the NFs. Our analysis found that ~ 27.8 wt% of ZnO has remained in the NPs and ~ 4.1 wt% retained in the NFs (calculated by subtracting 1.1 wt% of PAN from 5.2 wt% of ZIF-7/PAN). That is, we determined that $\sim 14.7\%$ of ZIF-7 NPs were initially embedded in the ZIF-7/PAN NFs. The estimated ZIF-7 loading value is in good agreement with the composition ratio opted in the initial synthesis process.

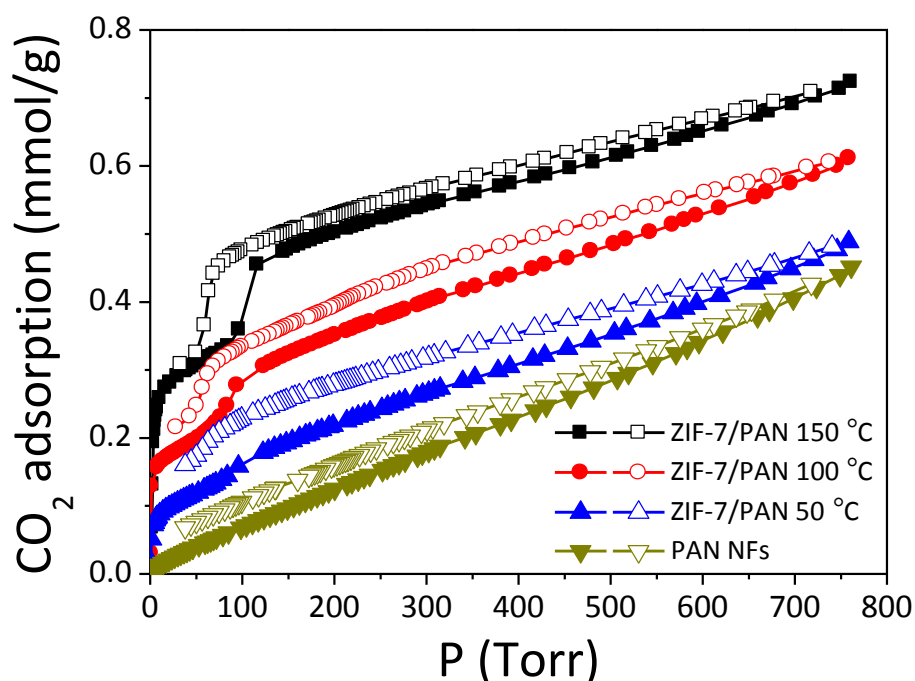


Figure 6. Adsorption/desorption isotherms of CO_2 (at 196 K) on ZIF-7/PAN NFs synthesized at the different temperatures of 50, 100, and 150 °C. Closed symbols represent adsorption and open symbols desorption. All samples were evacuated at 150 °C for 3 h prior to sorption studies to remove entrapped solvents and moisture.

The hysteresis of the adsorption/desorption isotherms of CO_2 on ZIF-7/PAN NFs synthesized at different synthesis temperatures are presented in Figure 6. Increasing synthesis temperature is supposed to affect the formation of ZIF, which is hereby confirmed *via* the CO_2 adsorption results. With an increasing synthesis temperature, the formation of ZIF-7 is

promoted (as explained in the XRD analysis, see Figure 4) resulting in a markedly higher CO₂ adsorption capacity. Even though 50 °C is a temperature sufficient to crystallize ZIF-7, as evidenced by the solvothermal synthesis of the NPs, we established that 50 °C is not adequate to fully develop ZIF-7 in the NFs because the crystallization process is likely to be suppressed by the PAN polymer (Figure 1(a)). However, it is not possible to increase the temperature above 150 °C because DMF contained in the ZIF-7/PAN solution will evaporate at higher temperatures during the synthesis process. As observed in Figure 6, the ZIF-7/PAN NFs exhibit a stepwise CO₂ adsorption behavior at ~100 Torr (196 K) because of the transformation of narrow pores in the ZIF-7 structure to a larger pore configuration (gate-opening effect¹¹) after the stimulus of CO₂. These results are in good agreement with experimental data of Bergh *et al.*³⁵ determined at 195 K. On the contrary, there is no step change in CO₂ adsorption for neat PAN NFs (without ZIF-7). Importantly, it is evident that the magnitude of stepwise increase in CO₂ uptake of the ZIF-7/PAN NFs is becoming more prominent with rising synthesis temperature, i.e. 150 > 100 > 50 °C. This finding supports the notion that the lesser adsorption of CO₂ is due to under developed ZIF-7 phase formed at a relatively lower synthesis temperature (in presence of PAN). The measured CO₂ adsorption in case the synthesis has been performed at 150, 100, and 50 °C cases at 760 Torr is about 0.72, 0.61, and 0.49 mmol/g, respectively, whereas ~4.9 mmol/g of CO₂ adsorption is observed in case of ZIF-7 NPs (Supplementary Information, Figure S1). The comparative study of CO₂ adsorption on ZIF-7 NPs and ZIF-7/PAN NFs shows that about 10–15 wt% of ZIF-7 NPs are present on the NFs as the result of the one-step synthesis process. This is consistent with the results of the TGA analyses. We anticipate that the CO₂ adsorption capacity can be enhanced further by higher loadings of ZIF-7 NPs onto the fibers. The full desorption curves of CO₂ in ZIF-7/PAN NFs demonstrates the reusability of NF mats in reversible CO₂ capture or separation applications.

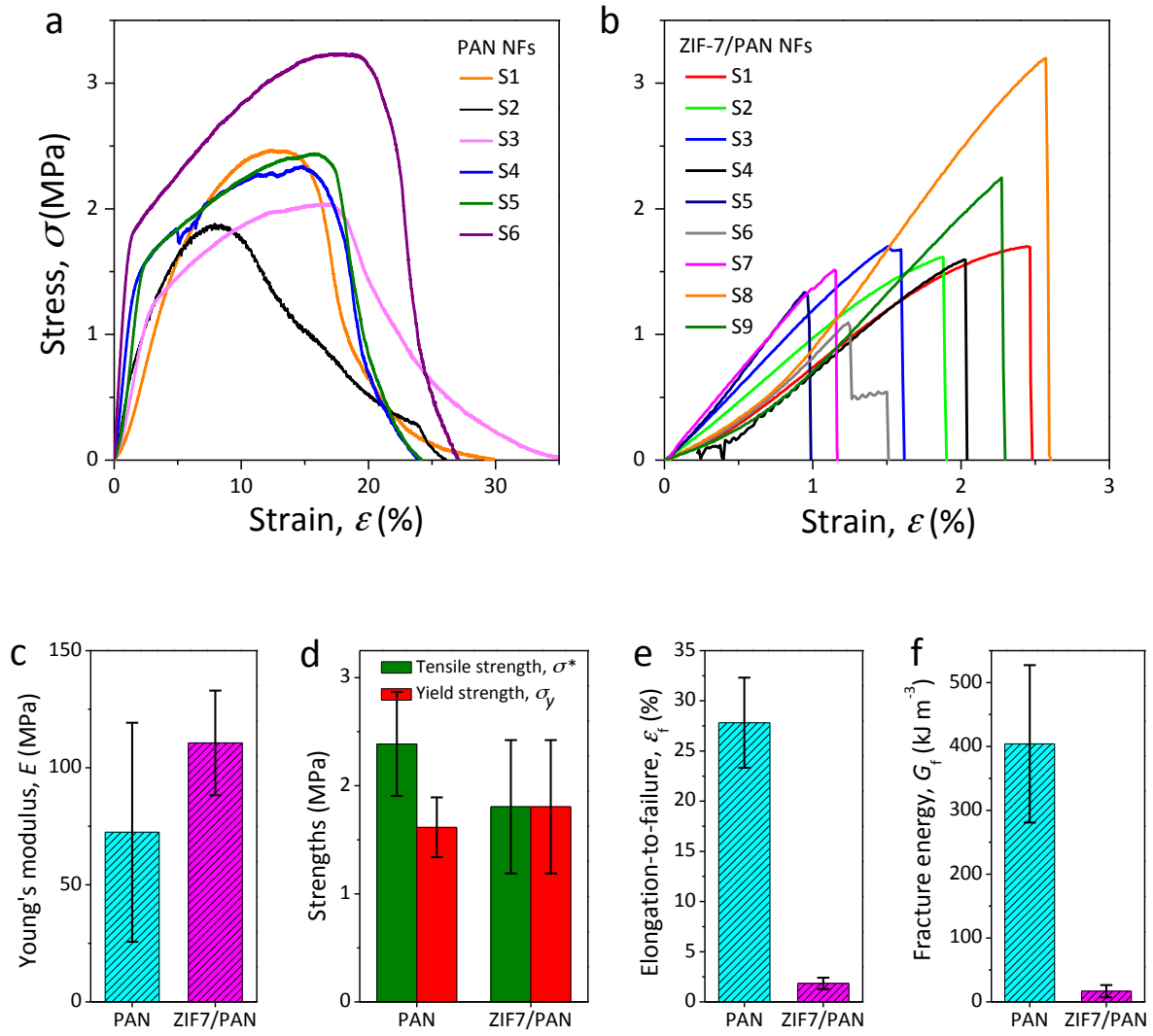


Figure 7. Nominal stress–strain curves measured under uniaxial tension for (a) PAN and (b) ZIF-7/PAN NF mats. The mechanical properties derived from the nominal stress–strain curves include: (c) Young’s modulus E that is a measure of the material stiffness, here determined from the gradient in the linear elastic region, corresponding to strains of < 1–2%. (d) Yield strength σ_y designating the level of stress after deviations from linearity start to develop, thus indicating the initiation of (irreversible) plastic deformation. Tensile strength σ^* marking the maximum nominal stress level. (e) Elongation-to-failure ϵ_f signifying the ‘ductility’ or ‘stretchability’ of the fiber material, right up to the point of fracture (breakage). (f) Fracture energy per unit volume G_f is a measure of the ‘toughness’ and corresponds to the damage tolerance of the material, calculated by integrating the area encompassed by the stress–strain curves from 0 to ϵ_f .

We have conducted large-strain uniaxial tensile deformation experiments on the NF mats, with and without ZIF-7, to establish the mechanical properties up to the point of material failure ϵ_f . Figures 7(a) and 7(b) present the nominal stress–strain data recorded from a representative number of individual test specimens, illustrating the material variability when subjected to mechanical loading based on the stochastic nature of the fiber architecture and its distribution. Noticeably, there is a considerable amount of plastic deformation accompanied by strain hardening when the mat is stretched beyond the elastic limit ($\epsilon \sim 1\text{--}2\%$), translating into a high ductility value of $\sim 28\%$ prior to fracture. On the contrary, it can be seen that plastic deformation has been suppressed after the inclusion of ZIF-7 NPs into the PAN matrix, which caused the ductility to decline substantially by one order of magnitude, approaching the level of $\sim 2\%$. It is clear that the mechanical deformation of the ZIF-7/PAN NFs can be considered to be brittle in nature (small ϵ_f) and rupture occurs more abruptly beyond the maximum stress σ^* . Such a ductile-to-brittle transition can be associated with the disrupted and discontinuous microstructure evidenced in the TEM images of the nanofibers (Figure 2), as opposed to pure PAN fibers. With respect to the Young's modulus and strength properties (Figures 7(c), 7(d)), however, we found that the differences between the neat PAN and ZIF-7/PAN NF mats are in fact small and could be accounted for by the relatively large error margins. Whereas the reduced ductility (Figure 7(e)) implies that the corresponding fracture energy (toughness, Figure 7(f)) will also be affected, in practice this might not pose a significant hindrance if the electrospun mats can be supported (e.g. encased or sandwiched) by means of a more robust substrate. Of course, another practicable strategy is to engineer the thin electrospun nanocomposite mats ($\sim 10\text{ s } \mu\text{m}$) to generate thicker laminated NF mats (e.g. $\sim 100\text{ s } \mu\text{m}$ to $\sim 1\text{ mm}$ in thickness, without degrading permeability), whose damage tolerance and mechanical stability will be enhanced.

Conclusions

In summary, we have developed a one-step process for the fabrication of ZIF-7/PAN NFs by electrospinning for the first time. The XRD characterization confirms the formation of ZIF-7 on the NFs and these composite NFs with the average diameter of 245 nm show markedly improved CO₂ adsorption and desorption characteristics, making them attractive for gas separation and other selective filtration applications. The CO₂ adsorption capacity can potentially be tuned or enhanced by controlling the wt% loading of ZIF-7 NPs embedded in the fiber. The proposed methodology of ZIF-7/PAN NFs fabrication is also scalable, enabling the production of large-size mats desirable for practical applications. The free-standing electrospun mats demonstrate reasonably good handleability, mechanical resilience and damage tolerance, thus paving the way for many useful industrial applications.

Acknowledgements

This work was supported by the Industrial Strategic Technology Development Program (10045221) funded by the Ministry of Knowledge Economy (MKE, Korea), NRF-2013M3A6B1078879, and NRF-2013R1A2A2A05005589. The authors extend their appreciation to the Deanship of Scientific Research at King Saud University for its funding this Prolific Research group (PRG-1436-03).

References

1. Li, J.-R.; Ma, Y.; McCarthy, M. C.; Sculley, J.; Yu, J.; Jeong, H.-K.; Balbuena, P. B.; Zhou, H.-C., *Coord. Chem. Rev.* **2011**, 255, 1791.
2. Drage, T. C.; Snape, C. E.; Stevens, L. A.; Wood, J.; Wang, J.; Cooper, A. I.; Dawson, R.; Guo, X.; Satterley, C.; Irons, R., *J. Mater. Chem.* **2012**, 22, 2815.
3. Davison, J.; Thambimuthu, K., *Proc. Inst. Mech. Eng., Part A* **2009**, 223, 201.
4. Yu, C.-H.; Huang, C.-H.; Tan, C.-S., *Aerosol Air Qual. Res.* **2012**, 12, 745.
5. Sumida, K.; Rogow, D. L.; Mason, J. A.; McDonald, T. M.; Bloch, E. D.; Herm, Z. R.; Bae, T.-H.; Long, J. R., *Chem. Rev.* **2011**, 112, 724.
6. Chaemchuen, S.; Zhou, K.; Kabir, N. A.; Chen, Y.; Ke, X.; Van Tendeloo, G.; Verpoort, F., *Microporous Mesoporous Mater.* **2015**, 201, 277.
7. Hwang, Y. K.; Hong, D. Y.; Chang, J. S.; Jung, S. H.; Seo, Y. K.; Kim, J.; Vimont, A.; Daturi, M.; Serre, C.; Férey, G., *Angew. Chem. Int. Ed.* **2008**, 47, 4144.
8. Horcajada, P.; Chalati, T.; Serre, C.; Gillet, B.; Sebrie, C.; Baati, T.; Eubank, J. F.; Heurtaux, D.; Clayette, P.; Kreuz, C., *Nat. Mater.* **2010**, 9, 172.
9. Park, K. S.; Ni, Z.; Côté, A. P.; Choi, J. Y.; Huang, R.; Uribe-Romo, F. J.; Chae, H. K.; O'Keeffe, M.; Yaghi, O. M., *Proc. Natl. Acad. Sci.* **2006**, 103, 10186.
10. Tan, J. C.; Bennett, T. D.; Cheetham, A. K., *Proc. Natl. Acad. Sci.* **2010**, 107, 9938.
11. Ryder, M. R.; Civalieri, B.; Bennett, T. D.; Henke, S.; Rudić, S.; Cinque, G.; Fernandez-Alonso, F.; Tan, J.-C., *Phys. Rev. Lett.* **2014**, 113, 215502.
12. Liu, S.; Xiang, Z.; Hu, Z.; Zheng, X.; Cao, D., *J. Mater. Chem.* **2011**, 21, 6649.
13. Lu, G.; Li, S.; Guo, Z.; Farha, O. K.; Hauser, B. G.; Qi, X.; Wang, Y.; Wang, X.; Han, S.; Liu, X., *Nat. Chem.* **2012**, 4, 310.
14. Zhu, M.; Srinivas, D.; Bhogeswararao, S.; Ratnasamy, P.; Carreon, M. A., *Catal. Commun.* **2013**, 32, 36.
15. Yue, Y.; Mehio, N.; Binder, A. J.; Dai, S., *CrystEngComm* **2015**, 17, 1728.
16. Liang, K.; Ricco, R.; Doherty, C. M.; Styles, M. J.; Bell, S.; Kirby, N.; Mudie, S.; Haylock, D.; Hill, A. J.; Doonan, C. J., *Nat. Commun.* **2015**, 6.
17. Cai, W.; Lee, T.; Lee, M.; Cho, W.; Han, D.-Y.; Choi, N.; Yip, A. C. K.; Choi, J., *J. Am. Chem. Soc.* **2014**, 136, 7961.
18. Yao, J.; Wang, H., *Chem. Soc. Rev.* **2014**, 43, 4470.
19. Breck, D. W., *Zeolite molecular sieves: structure, chemistry and use*; Wiley: New York, 1974.
20. Gücüyener, C.; van den Bergh, J.; Gascon, J.; Kapteijn, F., *J. Am. Chem. Soc.* **2010**, 132, 17704.
21. Li, Y.; Liang, F.; Bux, H.; Yang, W.; Caro, J., *J. Membr. Sci.* **2010**, 354, 48.
22. Fan, L.; Xue, M.; Kang, Z.; Li, H.; Qiu, S., *J. Mater. Chem.* **2012**, 22, 25272.
23. Tanh Jeazet, H. B.; Staudt, C.; Janiak, C., *Dalton Trans.* **2012**, 41, 14003.
24. Ostermann, R.; Cravillon, J.; Weidmann, C.; Wiebcke, M.; Smarsly, B. M., *Chem. Commun.* **2011**, 47, 442.
25. Lange, L.; Ochanda, F.; Obendorf, S. K.; Hinestroza, J., *Fibers Polym* **2014**, 15, 200.
26. Kang, C.-H.; Lin, Y.-F.; Huang, Y.-S.; Tung, K.-L.; Chang, K.-S.; Chen, J.-T.; Hung, W.-S.; Lee, K.-R.; Lai, J.-Y., *J. Membr. Sci.* **2013**, 438, 105.
27. Zhang, W.; Wu, Z.-Y.; Jiang, H.-L.; Yu, S.-H., *J. Am. Chem. Soc.* **2014**, 136, 14385.
28. Wu, B.; Pan, J.; Ge, L.; Wu, L.; Wang, H.; Xu, T., *Sci. Rep.* **2014**, 4.
29. Biswal, B. P.; Bhaskar, A.; Banerjee, R.; Kharul, U. K., *Nanoscale* **2015**, 7, 7291.
30. Bechelany, M.; Drobek, M.; Vallicari, C.; Chaaya, A. A.; Julbe, A.; Miele, P., *Nanoscale*

- 2015**, 7, 5794.
31. Huang, X.; Zhang, J.; Chen, X., *Chin. Sci. Bull.* **2003**, 48, 1531.
 32. Lu, G.; Farha, O. K.; Zhang, W.; Huo, F.; Hupp, J. T., *Adv. Mater.* **2012**, 24, 3970.
 33. Stassen, I.; Styles, M.; Greci, G.; Van Gorp, H.; Vanderlinden, W.; De Feyter, S.; Falcaro, P.; De Vos, D.; Vereecken, P.; Ameloot, R., *Nat. Mater.* **2015**.
 34. Tan, J. C.; Cheetham, A. K., *Chem. Soc. Rev.* **2011**, 40, 1059.
 35. van den Bergh, J.; Gücüyener, C.; Pidko, E. A.; Hensen, E. J. M.; Gascon, J.; Kapteijn, F., *Chem. - Eur. J.* **2011**, 17, 8832.
 36. Li, F.; Bao, X. X.; Yu, X. F., *Korean Chem. Eng. Res.* **2014**, 52, 340.
 37. Ma, G.; Yang, D.; Nie, J., *Polym. Adv. Technol.* **2009**, 20, 147.
 38. Bennett, T. D.; Keen, D. A.; Tan, J. C.; Barney, E. R.; Goodwin, A. L.; Cheetham, A. K., *Angew. Chem.* **2011**, 123, 3123.
 39. Du, Y.; Chen, R. Z.; Yao, J. F.; Wang, H. T., *J. Alloys Compd.* **2013**, 551, 125.